Load alleviation of feather-inspired compliant airfoils for instantaneous flow control

Bioinspiration & Biomimetics

PAPER

Load alleviation of feather-inspired compliant airfoils for instantaneous flow control

RECEIVED
10 February 2020

REVISED
19 May 2020

ACCEPTED FOR PUBLICATION
10 June 2020

PUBLISHED
6 October 2020

Lawren L Gamble[1], Christina Harvey and Daniel J Inman

Department of Aerospace Engineering, University of Michigan, Ann Arbor, United States of America
[1] Author to whom any correspondence should be addressed.

E-mail: llgamble@umich.edu

Keywords: load alleviation, passive morphing, morphing aircraft, feathers, compliant airfoil, flow control

Abstract

Birds morph their wing shape to adjust to changing environments through muscle-activated morphing of the skeletal structure and passive morphing of the flexible skin and feathers. The role of feather morphing has not been well studied and its impact on aerodynamics is largely unknown. Here we investigate the aero-structural response of a flexible airfoil, designed with biologically accurate structural and material data from feathers, and compared the results to an equivalent rigid airfoil. Two coupled aero-structural models are developed and validated to simulate the response of a bioinspired flexible airfoil across a range of aerodynamic flight conditions. We found that the bioinspired flexible airfoil maintained lift at Reynolds numbers below 1.5×10^5, within the avian flight regime, performing similarly to its rigid counterpart. At greater Reynolds numbers, the flexible airfoil alleviated the lift force and experienced trailing edge tip displacement. Principal component analysis identified that the Reynolds number dominated this passive shape change which induced a decambering effect, although the angle of attack was found to effect the location of maximum camber. These results imply that birds or aircraft that have tailored chordwise flexible wings will respond like rigid wings while operating at low speeds, but will passively unload large lift forces while operating at high speeds.

1. Introduction

Engineers frequently look to nature for inspiration regarding challenging problems. Within aerospace engineering, birds are a key inspiration due to their similarities to small unmanned aerial vehicles (UAV) in size, Reynolds numbers (Re), and flow speeds (V). Both operate within the atmospheric boundary layer and are subject to similar aerodynamic disadvantages due to the relative magnitude between gust and flight speed. These disadvantages, when compared to high altitude fliers, include larger changes in true air speed, acceleration, sideslip angles and increased directional sensitivity to perturbations and gusts [1]. Birds are able to mitigate the effects of these in-flight disturbances by changing their morphology.

1.1. Active morphing in avian and engineered wings

Biologists have long observed and recorded birds, which typically fly at $1 \times 10^5 < \mathrm{Re} < 4 \times 10^5$, actively controlling their flight through morphing wing and tail maneuvers [2]. Early studies have identified a vast array of maneuvers that birds use to control flight. For example, shifting the wing fore or aft of the center of gravity is used as a means of pitch control [3], fulmars use wing rotation about the shoulder to produce rapid vertical translations and is typically implemented in gusty conditions [3], wing flexion increases with flight speed [4], and wing span is tailored to increase performance [5].

Recent studies have begun to quantify some of these active effects with the aid of modern sensors. With such measurements, specific wing and tail maneuvers have been correlated to changes in attitude. For example, in-flight measurements of a steppe eagle's tail have demonstrated that it controls pitch with prolonged tail maneuvers while rapid small-amplitude tail maneuvers are hypothesized to be corrective measures in response to turbulence [6]. An experimental and observational study showed that gulls flex their elbow angle as wind speed increases allowing them to adjust their static pitch stability [7]. Further, in-flight surface reconstructions of wing camber showed that wing tip camber asymmetry is used to alleviate roll rates [8].

Engineers have attempted to harness the controllability and efficiency of birds by designing bio-inspired active morphing mechanisms. Such active morphing airfoil designs have focused on airfoil camber morphing, this includes the variable camber continuous trailing edge flap (VCCTEF) [9], spanwise morphing trailing edge (SMTE) [10], fish bone active camber (FBAC) [11], and synergistic smart morphing aileron (SSMA) [12]. Even more novel morphing actuators have been developed, such as biomimetic feather flaps, which alleviate gust loadings when actively deployed [13]. These concepts rely on actively control lift, pitch, and roll by adjusting camber via smooth changes in wing geometry. These and other morphing mechanisms aim to surpass their rigid counterparts with increased control authority, reduced drag [10], increased efficiency [14], reduced weight, and rapid response times [12].

1.2. Passive morphing in avian and engineered flight

While active morphing has received a lot of attention from biologists and engineers, studies have also suggested that passive morphing is prevalent in nature and can provide aerodynamic benefits. Passive morphing does not rely on sensors, controllers, and actuators, thereby reducing the response time such that it is practically instantaneous. Hummingbird wings experience negative camber during the downstroke and positive camber during the upstroke which provides efficient lift generation when coupled with wing twist [15]. In gliding flight, passive mechanisms are often much subtler. While landing, the wings of eagles deploy covert feathers as a leading edge flap which decreases the stall speed and augments lift production [16]. Large soaring birds such as hawks and eagles are known to have emarginated primary feathers which deflect upwards in soaring flight. This has been found to reduce induced drag but at the cost of increased parasitic drag [17, 18].

Despite previous research into these passive mechanisms, relatively little is known about the fluid–structure interaction of secondary feathers which cover the in-board trailing edge of bird wings (figure 1). Bachmann *et al* conducted wind tunnel testing on a hybrid airfoil with secondary feathers embedded into the trailing edge and demonstrated that the secondary feathers decamber with increased wind loadings but were not able to comprehensively quantify this effect [19]. Furthermore, Nachtigall *et al* measured the decambering of a pigeon's airfoil in flight [20]. These feathers are highly flexible and understanding the potential costs and benefits of this flexibility can provide new avenues of bio-inspired investigation for engineers.

Research into flexible airfoils has traditionally been geared towards membrane wings or oscillating motions in pitch and/or plunge due to either spanwise aeroelasticity or flapping motions. These studies

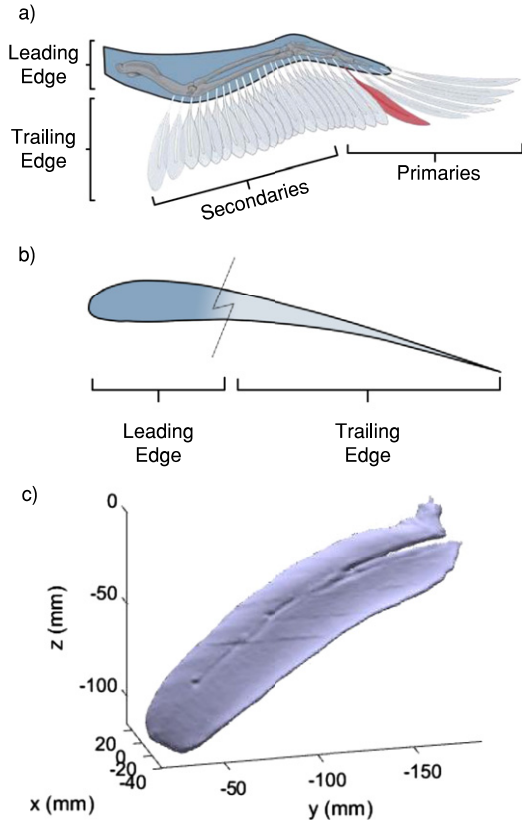

Figure 1. Bird wing anatomy of (a) a partially extended wing with traditional aircraft terminology and P5 feather highlighted (b) approximate airfoil shape at secondaries upon full wing extension. (c) Orthogonal view of the scanned profile of the 5th primary feather.

focus on the low Re regime ($Re < 5 \times 10^5$) which encompasses the Re range of natural fliers like birds. Initial chordwise flexible airfoil studies were conducted by Kim and Lee who developed an analytical model which coupled a doublet lattice method with a finite beam method and two spring elements in order to assess the aeroelastic effects of a flexible plate experiencing pitch and plunge motions [21]. This work was followed by Shyy *et al* who studied the effects of turbulence and aerodynamic performance of a flexible membrane-based airfoil in low Re flow [22–25]. Similar research numerically simulated and experimentally tested the fluid–structure interactions of flexible airfoils with feather-like trailing edges undergoing pitch and plunge motions in low Re flow [26–28]. These experiments determined that flexibility of oscillating airfoils reduces the effective angle of attack due to decambering while increasing thrust. Finally, research by Relvas and Suleman formulated an aeroelastic model using corotational structural elements to simulate the airfoil skin coupled with a fluid model which incorporated moving reference frames to model a flexible airfoil undergoing a prescribed harmonic pitching motion [29]. This method is promising in dynamic analyses as the fluid mesh does not require regeneration given small structural displacements, saving computational time. One

of the most relevant characteristics observed in many of these studies is that the flexible airfoils experienced less fluctuations in lift force, a trait which may be especially useful for gust mitigation and suppressing separation for low-altitude fliers [30, 31].

2. Problem overview

The primary objective of this work is to investigate the steady aero-structural effects of passive camber morphing of a bio-inspired 2D flexible airfoil. This analysis is done using bird wings as a starting point. Bird wings and feathers exhibit largely non-uniform material properties in both the spanwise and chordwise directions. This work couples a nonlinear corotational finite element method with XFOIL, a vortex panel based computational fluid method, to develop a fluid–structure interaction (FSI) model used for assessing a 2D flexible airfoil. The resulting XFOIL-corotational (XCO) model follows a similar but unique method to the work developed by Relvas and Suleman for dynamic pitch and plunge motions [29]. Unlike prior studies which have focused on the use of flexible airfoils in dynamic flapping maneuvers (i.e. pitching and heaving) with uniform material properties, we assess the steady aerodynamic response of a flexible airfoil with non-uniform chordwise properties. While dynamic flapping motion draws many parallels with biological fliers, its applicability to aircraft larger than micro air vehicles is limited. As such, the current work was conducted through a bioinspired lens with the goal of further advancing the knowledge of how feather flexibility may affect gliding birds as well as to inform low-altitude UAV design. In particular, three main questions will be answered. First, we investigated how aerodynamic loads deform the flexible airfoil shape. Next, we quantified how the resultant deformations in turn affect the aerodynamic load production of the airfoil. Finally, we investigated the possibility of replicating these deformations in a flexible 3D printed airfoil.

It is important to consider the composition of a bird wing to permit comparison to aircraft wings. For simplicity, bird wings may be thought of as two main sections along the cross section (figure 1(b)). The leading edge is the front portion of the wing and comprises a complex system of bones, muscles, skin, small covert feathers and ligaments. In contrast, the trailing edge is composed of a series of overlapping flight feathers which provide a lightweight lifting surface. The leading edge ligament, skeletal structure, and flight feathers are considered analogous to the leading edge, spar, and trailing edge of a traditional aircraft wing, respectively, for the purpose of this study. The flight feathers consist, in part, of the primary and secondary feathers. Secondary feathers make up the inboard section of the wing, with the root of each feather's shaft directly embedded into indentations in the ulna. All secondary and primary feathers are attached at their shafts by a ligament called the vinculum [32, 33]. We selected to model the secondary feathers as a cantilevered structure, where the fixed end is secured to the ulna and the other end remains free. It is important to note that for oncoming flow, secondary feathers rachides are predominantly oriented parallel to the flow while the primary feathers are oriented with increasing perpendicularity.

2.1. Structural feather characteristics

In order to assess the passive deformations of feathers, an understanding of their composition, geometry and material properties is crucial. Feathers are composed of multiple keratin structures including the shaft, vane, barbs and barbules [34]. The main shaft is composed of the rachis which supports the feather vanes and the calamus which is embedded into the skin and bone [35]. The shaft exterior is made of a thick layer of cortex, and filled with a sponge-like medullary material. Removing the medulla was found to only have a minimal effect on a feather's bending properties and as such, we assumed that its contributions were negligible in our study [34]. As the cortex tapers towards the tip, it varies from an oval shape near the feather base to a rectangular shape near the tip [35]. This directly affects the second moment of area ($I(x)$) along the shaft, which is at its maximum located near the feather's root. Studies have shown that the Young's modulus ($E(x)$) of feather keratin is largely conserved across species [34, 36]. However, within a single feather the Young's modulus may be slightly higher at the tips, which is primarily due to the arrangement of the keratin fibers [35].

In our model we selected to only model the feather flexibility with the properties of the rachis without the vanes. We chose to do this because few studies on the structural properties of the feather's vane have been conducted. The vane consists of a complex hierarchical structure of barbs which branch into barbules that use hooklets to form an interlocking Velcro-like structure [37] which is difficult to model. Lastly, the vane of individual secondary feathers has been shown to generate weak restoring moments to out-of-plane loadings, indicating its structural effects are not predominant [37].

With this background in mind, we modelled a flexible airfoil based on an avian feather using a few key assumptions. First, direct measurements of the chordwise distribution of Young's modulus and second moment of area of a barn owl's 5th primary feather rachis were used as the airfoil's trailing edge structural properties in this analysis [34]. As the Young's modulus has been demonstrated to be relatively consistent across species, it is reasonable to assume that this consistency extends to primary and secondary feathers. Our study does not include

any potential contributions of the surrounding feathers to the structural rigidity. This simplifies the analysis by removing the complexity of modelling the interaction between the Velcro like vanes. Lastly, no numerical data was available for the cross sectional area ($A(x)$); however, Bachmann's work included digital profiles of the feather cross section, excluding the medulla, from photographic measurements. We processed those images in MATLAB to quantify the cross sectional area along the feather shaft.

Differences in both the size, cross sectional area and the second moment of area between secondary and primary feathers likely exist but have not been comprehensively quantified. Photographic data from the U.S. Fish and Wildlife Service's Wildlife Laboratory indicates that the rachis of the barn owl's fifth primary is approximately 30% longer than that of the first to third secondary feathers while the vane length is 20% larger [38]. While this information is useful to understanding key differences between the two feather types, it is not possible to draw direct conclusions on secondary feather material properties. Given the limitations of currently available data, the assumption that secondary feathers exhibit the same chordwise material properties as primary feathers provides a useful first approximation of an avian-inspired flexible airfoil.

3. Methods

We used a coupled nonlinear fluid–structure formulation to model the flexible airfoil's aeroelastic response. Recent work in flexible airfoils has focused on the static and dynamic gust response. Murua derived analytical expressions to characterize the dynamic gust response of flexible airfoils; however, the finite element analysis was limited to a maximum of 3 degrees of freedom including pitch, plunge, and camber, the latter of which was restricted to small changes in camber which were dictated by prescribed parabolic shape functions [39]. Sucipto *et al*, compared a high-fidelity FSI simulation to a tuned low-fidelity semi-analytical simulation of a flexible airfoil's static and dynamic gust response and demonstrated good agreement between the two, provided that the flow remained attached [40]. Similarly, these simulations modeled the airfoil's displacement by assuming continuous material properties, small displacements, and that the camber was dictated by a Rayleigh beam element with Chebyshev polynomial mode shapes.

The following section details the aerodynamic and finite element models, the airfoil geometry, and the system coupling scheme that formulates the two-way weakly-coupled FSI algorithm implemented in our study. This model builds further upon existing studies by incorporating variable material properties, large displacements, and customized camber without assumed mode shapes. The FSI model was written in MATLAB which allowed for rapid coupling between the fluid and structure model and easy parameterization. Lastly, the model was validated against simulations using commercially-available software (appendix A).

3.1. Fluid modeling

The numerical method in this model harnessed the open-source software XFOIL, a vortex panel based algorithm coupled with an integral boundary layer which is capable of rapidly evaluating viscid and inviscid flows of subcritical airfoils [41]. There are some limitations to XFOIL that should be addressed in the context of the present study. At low Re (below approximately 5×10^5 [42]), XFOIL has been found to over predict the lift coefficient and under predict the drag coefficient. Convergence may not be obtained in cases with full separation [43].

XFOIL outputs the aerodynamic lift, drag, pitching moment, and distributed pressure coefficients for a given airfoil shape. The distributed loading (in units of N m^{-1}) over each panel in the airfoil's mesh was calculated from the non-dimensional pressure coefficient using the following relation:

$$P = \frac{1}{2} C_p V^2 s \rho \tag{1}$$

where C_p represents the pressure coefficient, V represents the flow speed, ρ represents the air density, and s represents the section span. For this model, the span is set to the rachis' root thickness of 3.3 mm. This was required since the structural properties of the feather rachis are three dimensional and cannot be normalized by the local rachis width due to its complex variable geometry. To be clear, this model does not include 3D finite wing effects. Lastly, the direction of the pressure loading is oriented normal to each panel which is accounted for when coupling the aerodynamic forces and structural models.

3.2. Structural modeling

One caveat to modeling morphing structures is their inherent flexibility and potential to undergo large deformations. This introduces geometric nonlinearities into the problem formulation as the structural equations must be written relative to the deformed structure and the loads are now dependent upon the deformed geometry. As a result, the equilibrium equations must be solved relative to the deformed state. Written mathematically, the structural equations $KU = F$ are in fact $K(u)U = F(u)$ where both the stiffness matrix K and the load vector F are functions of the global displacements u. The corotational beam method provides a suitable finite element formulation for arbitrarily large displacements and rotations in the global coordinate system of geometrically nonlinear structures by decomposing the deformation into the rigid body motion and the small elastic deformations. The formulation for

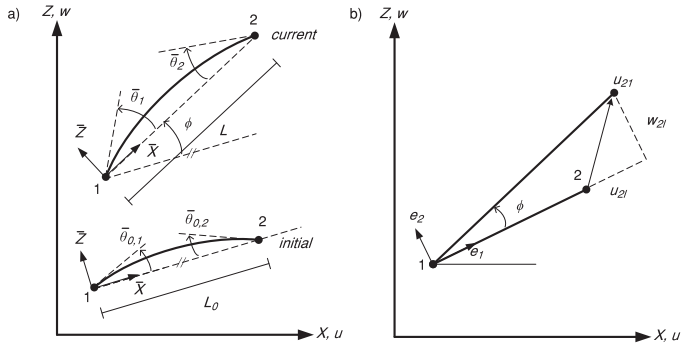

Figure 2. (a) Initial and current configuration of corotational beam element (b) infinitesimal local displacement from current configuration.

2D corotational beam elements is detailed succinctly below for completeness, following the derivation presented by Crisfield [?].

The corotational formulation defines a local element's coordinate system with its origin at the first node such that the coordinate system rotates with the element. Thus, the element's deformation-induced strain is discernible from the rigid body motion of the structure. The coordinate systems of both an initial (undeformed) and current (deformed) element are visualized in figure 2. Note that the local degrees of freedom $\overline{u}_1, \overline{w}_1, \overline{w}_2$ are zero since the local coordinate system rotates with the element and the origin is located at node 1. With this foundation, axial deformations and forces are calculated as:

$$\overline{u} = (L - L_0)\frac{L + L_0}{L + L_0} = \frac{L^2 - L_0^2}{L + L_0} \tag{2}$$

$$N = \frac{EA\overline{u}}{L_0} \tag{3}$$

where the local displacement $\overline{u}$ has been conditioned by $L + L_0/L + L_0$. This numerical technique ensures successful numerical calculations when the difference between L and L_0 is small. The initial and current element lengths can be derived geometrically as:

$$L_0 = \sqrt{(X_2 - X_1)^2 + (Z_2 - Z_1)^2} \tag{4}$$

$$L = \sqrt{((X_2 + u_2) - (X_1 + u_1))^2 + ((Z_2 + w_2) - \ldots \overline{(Z_1 + w_1))^2}} \tag{5}$$

where the current element length accounts for the global nodal displacements u, w. Now considering the flexural deformations of the element, the local end moments $\overline{M}_1$ and $\overline{M}_2$ can be written as a function of the local nodal rotations $\overline{\theta}_1$ and $\overline{\theta}_2$:

$$\begin{Bmatrix} \overline{M}_1 \\ \overline{M}_2 \end{Bmatrix} = \frac{2EI}{L_0}\begin{bmatrix} 2 & 1 \\ 1 & 2 \end{bmatrix}\begin{Bmatrix} \overline{\theta}_1 \\ \overline{\theta}_2 \end{Bmatrix} \tag{6}$$

where $\overline{\theta}_1$ and $\overline{\theta}_2$ are defined by

$$\overline{\theta}_\mathrm{i} = \theta_\mathrm{i} - \phi - \overline{\theta}_{0,\mathrm{i}} \tag{7}$$

where ϕ represents the element's rigid rotation and θ_0 represents the initial slope in the local coordinate system. At this stage, the set of non-zero local variables are assembled in vector format where $\overline{\mathbf{a}}^\mathrm{T} = (\overline{u}, \overline{\theta}_1, \overline{\theta}_2)$. The system of equations detailing the element forces can now be assembled:

$$\begin{Bmatrix} \overline{N} \\ \overline{M}_1 \\ \overline{M}_2 \end{Bmatrix} = \frac{E}{L_0}\begin{bmatrix} A & 0 & 0 \\ 0 & 4I & 2I \\ 0 & 2I & 4I \end{bmatrix}\begin{Bmatrix} \overline{u} \\ \overline{\theta}_1 \\ \overline{\theta}_2 \end{Bmatrix} \tag{8}$$

Upon deriving the internal forces in the local coordinate system, the relationship between the global and local variables can be determined. This is approached through variational principles, considering a small variation in global displacement from the current configuration δu_{21}. The local axial displacement is calculated by projecting the global displacement onto the unit vector $\mathbf{e}_1 = (\cos\phi, \sin\phi)$ along the length of the element shown in figure 2.

$$\delta\overline{u} = \boldsymbol{e}_1^\mathrm{T}\delta\boldsymbol{u}_{21} = \begin{Bmatrix} \cos\ \phi \\ \sin\ \phi \end{Bmatrix}^\mathrm{T}\delta\boldsymbol{u}_{21} \tag{9}$$

Thus,

$$\delta\overline{u} = \begin{Bmatrix} \cos\ \phi \\ \sin\ \phi \end{Bmatrix}^\mathrm{T}\begin{Bmatrix} \delta u_2 - \delta u_1 \\ \delta w_2 - \delta w_1 \end{Bmatrix} \tag{10}$$

This can be written succinctly as:

$$\delta\overline{u} = \mathbf{v}^\mathrm{T}\delta\mathbf{a} \tag{11}$$

where $\mathbf{v}^\mathrm{T} = (-\cos\phi, -\sin\phi, 0, \cos\phi, \sin\phi, 0)$ and $\delta\mathbf{a} = (u_1, w_1, \theta_1, u_2, w_2, \theta_2)$ are the unknowns assembled in the global coordinate system.

The second unit vector $\boldsymbol{e}_2^\mathrm{T} = (-\sin\ \phi, \cos\ \phi)$ can now be used to derive the relationship between the local and global rotations. A small variation in angle can be calculated based on a change in arc length where $L\delta\phi = \boldsymbol{e}_2^\mathrm{T}\delta\boldsymbol{u}_{21}$ which can be rewritten in a

similar manner to equation (11) using the global unknowns

$$\delta\phi = \frac{1}{L}(\sin\ \phi, -\cos\ \phi, 0, -\sin\ \phi, \cos\ \phi, 0)\,\delta\boldsymbol{a} \tag{12}$$

Recalling that equation (7) defines the relationship between the rigid bar rotation and the slope in the global coordinate system, this can be rewritten to express the local nodal rotations in terms of the unknowns in the global coordinate system.

$$\begin{Bmatrix}\overline{\theta}_1\\ \overline{\theta}_2\end{Bmatrix} = \left(\begin{bmatrix}0&0&1&0&0&0\\0&0&0&0&0&1\end{bmatrix} - \frac{1}{l}\begin{bmatrix}\mathbf{z}^{\mathrm{T}}\\ \mathbf{z}^{\mathrm{T}}\end{bmatrix}\right)\delta\boldsymbol{a} \tag{13}$$

where $\mathbf{z}^{\mathrm{T}} = (\sin\phi, -\cos\phi, 0, -\sin\phi, \cos\phi, 0)$. From this equation, the rotation matrix can be inferred as:

$$\mathbf{B} = \begin{bmatrix}0&0&0&0&0&0\\0&0&1&0&0&0\\0&0&0&0&0&1\end{bmatrix} + \begin{bmatrix}\mathbf{v}^{\mathrm{T}}\\ -\frac{1}{l}\mathbf{z}^{\mathrm{T}}\\ -\frac{1}{l}\mathbf{z}^{\mathrm{T}}\end{bmatrix} \tag{14}$$

3.3. Airfoil geometry and mesh formulation

As mentioned in section 2.1, the airfoil geometry used in this analysis is based on biological wings. Many studies of bird wings use highly cambered high lift airfoils; however, generating consistent data with these airfoils at low Re (below 3×10^5) across experimental and simulated data at equivalent flow conditions has proven to be challenging [42, 44, 45]. In contrast, symmetric airfoils with a moderate thickness such as the NACA 0012, which are notably inappropriate for the current study, provide very consistent results across experiments and simulations both with and without viscous effects. A comprehensive analysis, detailed in appendix A.2.1 was conducted to determine an appropriate airfoil geometry by comparing the results of two fluid models: an inviscid vortex panel method, and XFOIL which includes viscous effects due to the boundary layer and wake. The purpose of this analysis was to identify an airfoil that drew parallels to highly cambered biological airfoils, but was expected to show good agreement between simulations and experiments. From this analysis, the NACA 6409 was chosen due to its similarity to moderately thin and cambered biological airfoils and because it showed fairly good agreement between the two models for pre-stall angles of attack for a range of Reynolds numbers. This comparison was verified against experimental measurements and numerical simulations in ANSYS, a commercially-available engineering software (section appendix A), and was shown to be within 11.5% of the experimental results. The surface of NACA 6409 was then discretized into a mesh with 200 panels for use in the FSI model.

The structural mesh used in the corotational method was defined in a different manner. Given the composition of the true bird wing mentioned prior, the airfoil's leading edge was assumed to be rigid in the chordwise direction for the purposes of this analysis. Furthermore, as mentioned in section 1, the trailing edge exhibits passive deformations and thus was assumed to be flexible. As such, the structural mesh used in the FEM model was composed solely of elements along the trailing edge and was modeled to represent the camber and function of a secondary feather. The two dimensional geometry of an unloaded feather was mapped using a NextGen 3D scanner which uses four twin Class 1M, 10 mW solid state lasers in addition to multistripe laser triangulation technology figure 1(c). This scanner is capable of regenerating surface geometries within 1/10 000th *m* accuracy in macro mode.

Table 1. Comparison of non-dimensional wind speeds across a spectrum of fliers. Species data from [46, 47].

Species	S(m)	c(m)	W(kg)
Red-tailed hawk	1.22	0.38	1.08
Barn owl	1.01	.017	0.46
Pigeon	0.68	0.098	0.549

As discussed earlier, the Young's modulus and second moment of area used in this analysis were taken from data on barn owl feathers [34]. However, we were not able to acquire specimens of barn owl feathers. Instead we scanned a red-tailed hawk specimen which has a slightly larger wingspan, chord length and body weight than the barn owl in order to measure the chordwise feather curvature (table 1). It is important to note that there are large species-specific differences in feather geometry, however this model provides an initial estimation of the effects of avian feather flexibility in gliding flight and does not directly comment on a specific species. The chord length of the airfoil was chosen to be 0.28 m, which is between that of the red-tailed hawk and the barn owl [46, 47]. The two-dimensional curvature of the first secondary feather was scaled and oriented so that the flexible part of the airfoil made up 60% of the chord. The feather's root was prescribed with fixed displacement and rotation boundary conditions. As such, the structural component of the trailing edge can be thought of as a flexible cantilevered beam with pre-curvature. Not only is this intended to represent a biological wing, but manufacturing a similar wing with a high Young's modulus trailing edge core embedded into a low-stiffness exterior material is easily achieved with multimaterial 3D printing. This algorithm can be easily adapted to model the entire airfoil skin with geometrically nonlinear corotational elements if desired for other engineering scenarios.

3.4. Coupling algorithm

The XCO model developed here uses an iterative Newton–Raphson solution method to model the nonlinear nature of the flexible airfoil (figure 3)

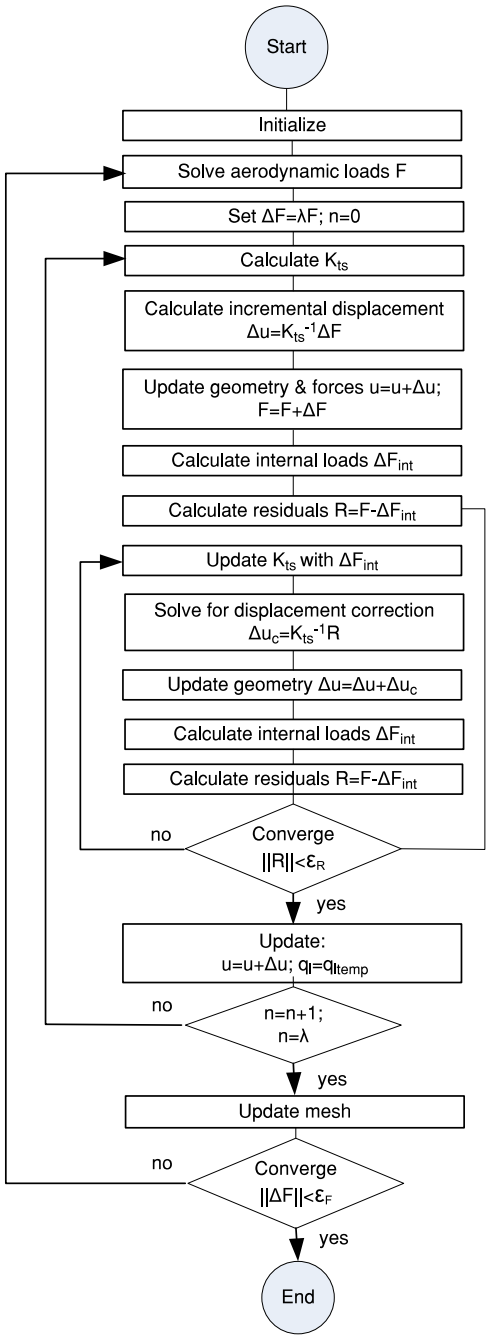

Figure 3. Flow chart of structural and aerodynamic integration.

under steady aerodynamic loads. First, the loads, displacements and meshes were initialized. The initial undeformed airfoil geometry was then passed to the fluid model which calculated the nondimensional aerodynamic pressure coefficient c_p for the desired angle of attack along the airfoil's surface. The total pressure acting normal to the structural elements was calculated by taking the pressure difference between the upper and lower trailing edge surface. This pressure distribution was interpolated at the nodes of each element using a linear pressure distribution across each element. The loading was then discretized into 25 incremental loads for the Newton–Raphson algorithm which were then used in conjunction with the tangential stiffness matrix to solve for the incremental displacements. The displacements were used to update the structure, and the residual internal loads in the structure were checked for convergence. If force convergence was not met, the tangential stiffness was updated using the incremental internal loads and the solution process was repeated until convergence was met. Upon convergence, the structural mesh was updated and the iterative process was repeated with the next load increment. Once the model has reached the final load increment, the structural and airfoil mesh were updated to reflect the converged displacements. Unless the norm of the converged forces falls below the specified tolerance of 1×10^{-6}, the new airfoil geometry was used to calculate the pressure loads and the iterative load process was repeated.

4. Results

4.1. Aerodynamic response

Here, we investigated the effects of variable angle of attack (pre-loaded) and Reynolds number on the flexible airfoil's pressure distribution, lift and trailing edge displacement. In total, thirteen different values of Re were tested between 0.2×10^5 and 5×10^5, corresponding to flow speeds ranging from 1.04 to 26.12 m s^{-1}. It should be noted that in this analysis, the effects of Reynolds number are only the result of changes in flow speed since the airfoil chord had a negligible extension is it decambered. The lift coefficient and chordwise pressure distributions are shown in figure 4. The low-Re regime ($Re < 1 \times 10^5$) is characterized by low pressure and lift coefficients, consistent with low-Re experiments [48]. The flexible airfoil's pre-stall lift distributions for values of Re between 1×10^5 and 2×10^5 show little to no distinction, indicating that the flexible airfoil is able to maintain aerodynamic performance (figure 4(a)). For Re greater than 2.5×10^5, the lift curve shifts downwards with increasing values of Re, mirroring other methods of passive load alleviation [49, 50]. Furthermore, we found that while the lift decreases at high Re, this did not substantially decrease the predicted maximum lift coefficient. A direct comparison of the lift and drag forces between the rigid and flexible airfoil is presented in figure 6. Furthermore, a delay in the stall angle is also observed, indicating that this passive mechanism may aid in maintaining flow attachment. This is supported by previous work which found that airfoils with reduced and reflexed camber experience a delay in stall angle [12]. Furthermore, like rigid airfoils, increasing the angle of attack linearly increases the lift coefficient prior to stall.

This can be further assessed by observing the chordwise distribution of the pressure coefficient shown in figure 4(b). We found that for Re below 1.5×10^5, the flexible and rigid airfoil exhibit visibly identical pressure profiles, again confirming

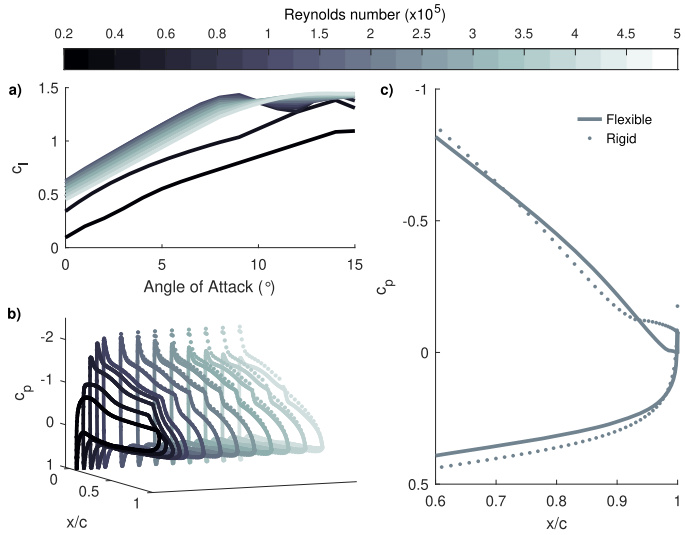

Figure 4. Effects of aeroelastic deformations on (a) lift coefficient and (b) chordwise pressure distribution for $\alpha = 6°$ with rigid solution shown in dashed lines (c) trailing edge pressure distribution over the rigid airfoil for Re $= 5 \times 10^5$, $\alpha = 11°$.

that the flexible airfoil behaves in a rigid manner in this regime. However upon increasing Re, the flexible airfoil begins to lose suction on the upper surface which causes the loss in lift observed in figure 4(a). We also found that the rigid airfoil undergoes trailing edge separation prior to the flexible airfoil, shown in figure 4(c). This is indicated by the plateau in pressure coefficient over the last 10% of the rigid airfoil's chord.

To further understand the load alleviation effects at high Re, we investigated two key parameters. First, we looked at the sectional lift curve slope, which is the change of lift force per change of angle of attack before stall (in the linear region, figure 5(a)). Next, we quantified the lift intercept, which represents the lift at 0° angle of attack (figure 5(b)). We found that the observed load alleviation was largely due to the decrease in the intercept relative to its rigid counterpart. This is due to the decambering of the airfoil which mirrors the effect of decreasing aileron deflection in traditional aircraft. Interestingly, the flexible airfoil had a higher lift slope than the rigid airfoil at the high Re numbers. Flexibility was shown to have little to no effect on either parameter below 1.5×10^5.

Both the airfoil thickness and camber have been shown by other researchers to affect the lift curve slope; however, these effects are not uniform across Reynolds numbers. Sunada [51] found that the lift curve slope was inversely related to the airfoil's thickness ratio and proportionally related to the airfoil's camber for Re of 4×10^3; however, these findings are contrary to the results of Abbott and Doenhoff [52] which were conducted at Re $> 1 \times 10^6$ and found the slope increased with thickness ratio. Abbott and Doenhoff also found that the slope increased with decreasing aileron angle. The flexible airfoil presented

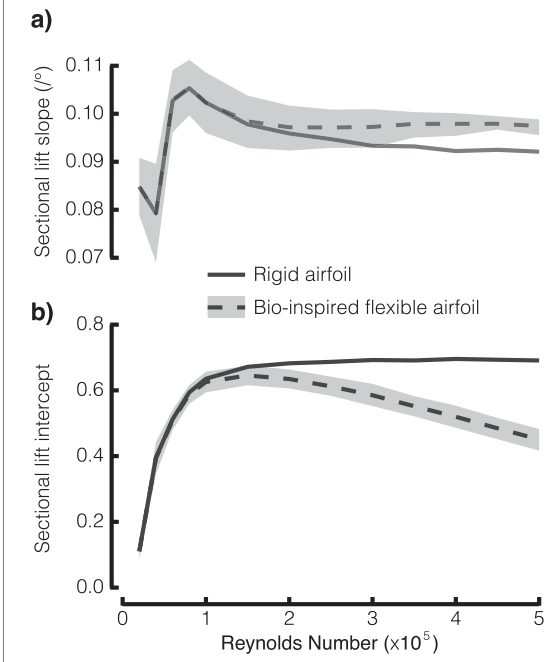

Figure 5. Sectional lift (a) slope and (b) intercept for small angles of attack in the linear region of the lift curve. The band of bioinspired airfoil data represents the minimum and maximum range of feather stiffness taken from error bars in [34].

in this work is analogous in many ways to a conventional aileron; thus, we believe the increase in slope is due to the decambered flexible trailing edge acting like an aileron with a reduction in actuation angle.

The difference in sectional aerodynamic forces between the rigid and flexible airfoils, shown in figure 6, further highlight how the aerodynamic loads are alleviated. Across all Re, the flexible airfoil produced less lift force than its rigid counterpart, though the effect is small at low Re. As the Reynolds number increased, we found that there was a larger

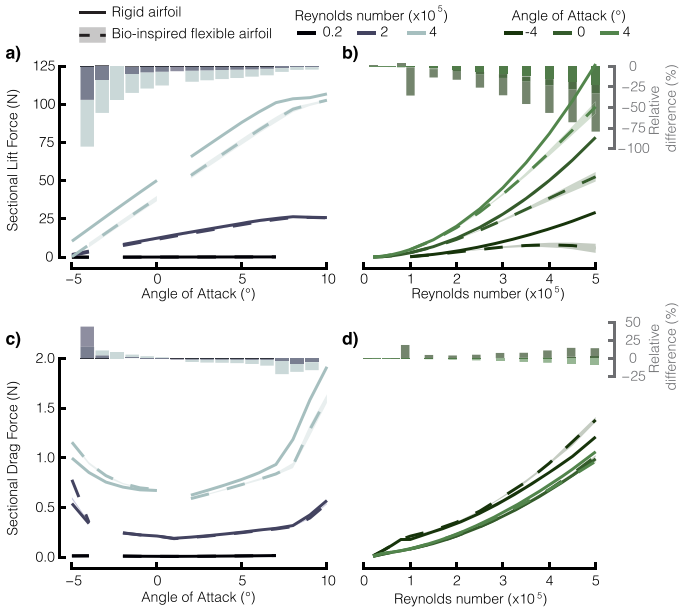

Figure 6. Aerodynamic lift force as a function of (a) angle of attack across constant Reynolds numbers with (b) relative difference of the flexible airfoil compared to the rigid airfoil and (c) lift response as a function of Reynolds number for constant angles of attack with (d) [see (b)].

relative reduction in the lift force. Although there was always a reduction of lift for a flexible airfoil, when the angle of attack was increased there was a smaller relative reduction of the lift force. For example, at $Re = 1.5 \times 10^5$ the flexible airfoil alleviated over 30% of the lift force generated for 0° angle of attack but only about 20% of the lift force generated for 4° angle of attack.

The drag profiles again show that the effects of flexibility are most predominant at higher Re; however, the effect depends on the angle of attack. Negative angles of attack see a slight increase in drag with a flexible airfoil (figures 6(c) and (d)) but high angles of attack see a large reduction in the sectional drag force. It should be noted that while the percent difference is a useful metric for quantifying the change between two similar quantities, small numerical values tend to exhibit large percentage differences due to the tendency of fractions with near-zero denominators to approach infinity. We attribute these results to the impact of the dynamic pressure on the aerodynamic force. Simply put, as the wind speed increases, the dynamic pressure and hence the aerodynamic loading on the airfoil increases quadratically. This allows the airfoil to maintain a semi-rigid configuration at lower wind speeds and passive unload aerodynamic loadings at higher wind speeds.

4.2. Structural response

To analyze the flexible airfoil shape change across all Re and angles of attack we used a principal component analysis (figure 7) which transforms a dataset of correlated variables into independent (principal) components. The resultant components capture the shape change of the trailing edge removing the effects due to translation, rotation or scaling. The first principal component (PC1) accounts for the largest possible variance in the dataset, while the second principal component (PC2) accounts for the highest variance possible while also being orthogonal to PC1. The advantage to this method is that it can capture changes in curvature that are difficult to quantify with classic airfoil variables such as the magnitude and location of maximum camber. For completeness, we also calculated these standard variables.

In our principal component analysis, we used 57 key landmarks along the flexible trailing edge of the airfoil in 2 dimensions. This analysis found that Re had a statistically significant positive effect on PC1 (effect $= 1.72 \times 10^{-8}$/Re, p-value < 0.001) while the angle of attack had a statistically significant positive effect on PC2 (effect $= 2.17 \times 10^{-5}/°$, p-value < 0.001). This indicates that the influence of Re and angle of attack on the airfoil's deformation act independently of one another. Note that these effects are calculated per unit of Re or angle of attack and thus, the differences in effect magnitudes are due to differences in the order of magnitude between Re (on the order of 10^5) and angle of attack (on the order of 10^1). Thus, the total effect of each parameter within our test range is determined by multiplying this value by the desired Re or angle of attack, respectively.

Furthermore, PC1 (and hence, the Re) was responsible for 99.7% of the observed shape change while PC2 (and hence, the angle of attack) was responsible for 0.3% of the observed shape change. In order understand how this shape change was expressed in the airfoil's deformation, we calculated the maximum camber and location of maximum

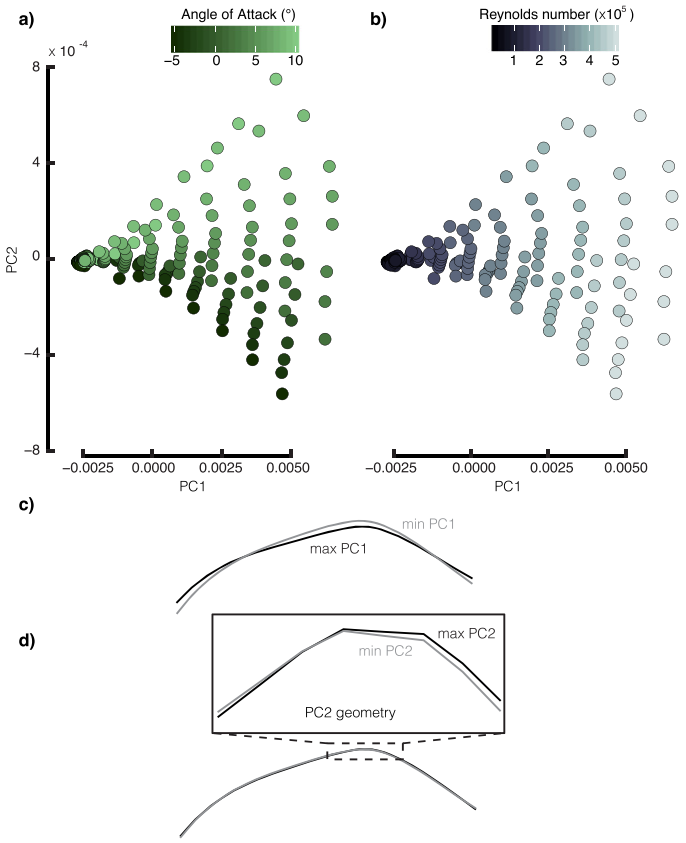

Figure 7. Principal component analysis for the (a) angle of attack response and (b) Reynolds number response. Geometric interpretation of the (c) 1st principal component and (d) 2nd principal component with a closeup to highlight the component change. Note that (c) and (d) are unitless representations of the deformed geometry.

camber for each deformed airfoil. This showed a linear positive relationship ($R_2 = 0.9996$) between the magnitude and location of maximum camber. By comparing the maximum camber and location of maximum camber to the principal components identified in our analysis, we found that an increase in both PC1 and PC2 was associated with a reduction and forward shift of the maximum camber. To summarize, while both Re and angle of attack capture a decrease and forward shift of the maximum camber, Re is correlated with the largest axis of variation (PC1) and is responsible for the majority of the shape change observed in our study while the angle of attack is correlated with the smaller axis of variation (PC2) and plays a minor role in the resultant shape change.

These trends are visualized by the colour gradients in figures 7(a) and (b). The vertical gradient in figure 7(a) indicates that the angle of attack is responsible for variations in PC2 but remains fairly constant with respect to PC1. In contrast, the data depicted in figure 7(b) shows a horizontal gradient with respect to Re, which thus is responsible for variations in PC1. Furthermore, figures 7(a) and (b) highlights that between an angle of attack of 1° and 2° there is a step increase in PC1 and decrease in PC2 at all Reynolds numbers. We found that the airfoil experienced a sudden decrease in the camber and forward shift of the location of the maximum camber when the angle of attack was increased from 1° to 2°. This sharp change in the camber as the airfoil transitions from near zero to positive angles of attack is analogous to a snap-through-like phenomenon. At this instance, the aerodynamic suction is moving from the lower surface of the airfoil to the upper surface. In a symmetric airfoil, this would occur at 0°; however, due to the NACA 6409 airfoil's positive camber, this transition occurs at a non-zero angle of attack.

Further we can investigate the trailing edge tip deflection which is a readily determinable parameter that can easily characterize the overall deformation of the flexible airfoil, as shown in figure 8. The contour plot in figure 8(a) supports our prior findings that show Re is largely responsible for the flexible airfoil's total deformation. This is demonstrated by the near-vertical slope of the contour lines. At small angles of attack the relationship is linear; however, the tip displacement re-cambers near stall where the flow begins to separate over the surface. The case with the greatest tip deflection and thus the most decambered configuration is achieved right before stall at an angle of attack of 8° and a Reynolds number of 5×10^5. At these conditions the maximum tip deflection is 6.5 mm, which corresponds to 2.3% of the airfoil chord. Figure 8(b) shows the relationship between the tip displacement and both Reynolds number and

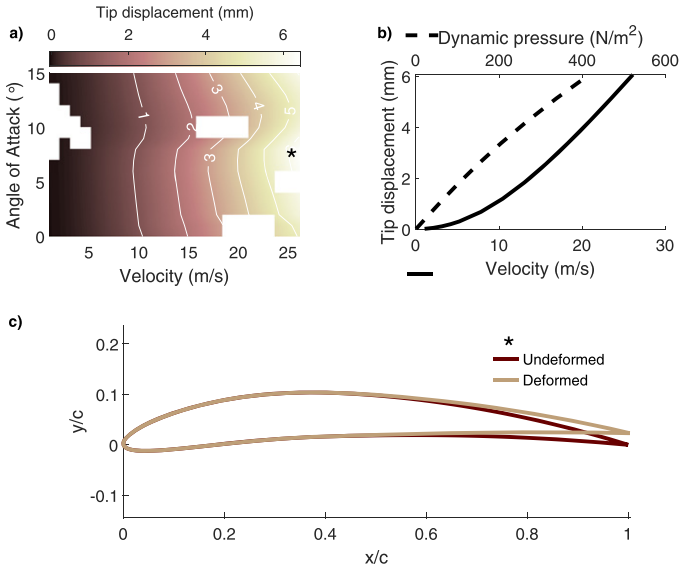

Figure 8. (a) Displacement contour plot (b) effect of dynamic pressure and Reynolds number on the tip displacement at an angle of attack of 15° and (c) deformed airfoil at an angle of attack of 15° and Reynolds number of 5×10^5.

dynamic pressure. Note that while the Reynolds number is a function of the flow velocity, the dynamic pressure is a function of the squared flow velocity. This, in part, explains the semi-quadratic relationship seen between flow speed and tip displacement (figure 8(b)).

Given these results, a few points should be noted. First, recall that this initial model simulates a single feather rachis for simple comparison to a 2D airfoil. In reality, the wing is composed of a series of overlapping feathers which is hypothesized to restrict the deformation of their neighboring feathers. Secondly, the feathers appear to be structurally stable up to a specific wind loading, after which the amount of deformation and associated change in lift increase more rapidly. Finally, it is important to recall that the lift force is a function of velocity squared. Thus, since the lift coefficient was shown here to be dependent upon velocity, this could indicate that the trailing edge flexibility acts as a method of passive gust alleviation to reduce the change in lift force and thus acceleration during transient aerodynamic conditions. This information can be useful when implementing bio-inspired flexible materials on the trailing edge of the wing. A feather-like structure will be able to maintain a known cambered shape with minimal deflections as the angle of attack is changed, whereas it may be tailored to improve aircraft performance across variable freestream velocities.

5. Reverse engineering a feather-inspired airfoil

Upon developing an understanding of how the pressure distribution and trailing edge flexibility interact, the chordwise flexibility of feathers can be reverse engineered to implement in a 3D printed airfoil or wing. The elemental stiffness of the feather was matched to the elemental stiffness of an engineered flexible trailing edge. Both the Young's modulus and the trailing edge thickness can be tailored to match the feather's chordwise stiffness properties. Any thickness can be 3D printed; however, the Young's modulus is a limiting factor in the airfoil's design and is heavily dependent upon the allowable materials of the 3D printer. For this application, an Objet Connex 500 multimaterial printer is used which can make multi-stiffness parts from two input materials. It utilizes liquid particle deposition like a typical inkjet printer in order to combine these two input materials in 10 different ratios. This printer is unique in that it can print a single integrated part with multiple stiffness in a single print job.

One difficulty in modeling the performance of soft 3D printed polymers is that their material properties are often not constant and vary with temperature, strain rate, etc [53]. In this application, Tango+, a flexible material, and Vero White, a rigid material, were used. The manufacturer provides some materials data for these polymer combinations, but Young's modulus data is only available for rigid materials. Experimental data of stress vs strain [53] was used to determine the Young's modulus of each of the possible material combinations at a strain rate of $1.2 \times 10^{-1}\ s^{-1}$ in the linear region of their strain curves. With this in mind, the algorithm is as follows. The objective function matched the bending stiffness of the 3D printed feather to the actual feather by tailoring the Young's modulus E and trailing edge thickness t. As the Young's modulus is a discrete variable, a solution map is created which shows how the predicted thickness varies with both location along the chord and the Young's modulus. This is solved by equating

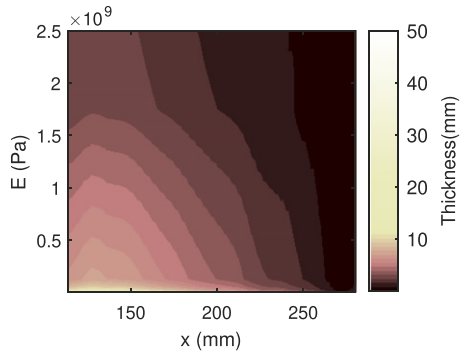

Figure 9. Solution map of trailing edge Young's modulus vs chordwise location, with the thickness plotted.

the stiffness terms for the 3D printed analog and the feather.

$$K_{\text{feather}}(x) = K_{\text{3D,print}}(x) \tag{15}$$

where

$$K_{\text{feather}}(x) = \frac{E_{\text{feather}}(x) * I_{\text{feather}}(x)}{d_{\text{feather}}} \tag{16}$$

and

$$K_{\text{3D,print}}(x) = \frac{E_{\text{3D,print}}(x) * h_{\text{3D,print}}(x)^3}{12} \tag{17}$$

Note that each expression has been normalized by the respective width for equivalence. Here, $K_{\text{feather}}(x)$ and $K_{\text{3D,print}}(x)$ represents the normalized flexural stiffness of the feather and 3D printed analog, respectively, and d_{feather} represents the diameter of the feather calamus.

Figure 9 shows the solution map. Note that the colour bar of the trailing edge thickness does not have a constant gradient, in part due to the drastic difference in stiffness properties between Tango+ and VeroWhite. A few trends can be noted from this map. The reduction in stiffness characteristics towards the tip of the feather's trailing edge is mirrored in the solution map. The predicted thickness, regardless of Young's modulus, tends to reduce along the trailing edge. This is most clearly observed in the purely elastomeric case which predicts a thickness of 40 mm at the root, to 2.5 mm at the tip.

The map indicates that there are many solutions to this problem which all produce the same structural response. There are three logical approaches to customizing the reverse engineered airfoil, each which have potential benefits and pitfalls depending on manufacturing and operating constraints. First, the map shows that a constant Young's modulus can indeed be used with reasonable thicknesses along the chord. The chordwise thickness would be determined by drawing a horizontal line at the desired Young's modulus. This approach would be useful in applications where a multimaterial printer is not readily available. Alternately, a constant thickness approach with tailored Young's modulus could be used. The chordwise Young's modulus would be determined by drawing a line following the color contour corresponding to the desired thickness. While requiring a multimaterial printer, this type of airfoil could be useful in applications where fatigue is a concern. While, both methods would be inappropriate for the existing analysis since the trailing edge geometry is not guaranteed to match that of the airfoil or feather rachis, they could be implemented in flexible trailing edge airfoils like those seen work by Shyy *et al* and Heathcote *et al* which have beam-like flexible trailing edges. Finally, the Young's modulus could be tailored along the chord such that the equivalent trailing edge thickness matches either the feather or the airfoil's trailing edge. The chordwise Young's modulus in this approach is determined by plotting the airfoil thickness versus the chord. The latter method would be the most appropriate option so that the lift and drag analysis conducted prior remains applicable.

6. Conclusions

In this work, the passive aeroelastic response of the secondary feathers of bird wings was investigated by developing and validating two fluid–structure interaction models of a bioinspired flexible airfoil. The loosely-coupled XCO model is computationally efficient and is able to rapidly assess a design space making it well suited for preliminary design and analysis. The higher-fidelity ANSYS model is more computationally costly but more accurately predicts experimental aerodynamic results, making it appropriate for final design analysis. Below Reynolds numbers of 1.5×10^5 which corresponds to flow speeds of 7.83 m s^{-1}, the flexible airfoil behaved similarly to its rigid counterpart. At higher Reynolds numbers, the flexibility of the airfoil induced substantial reductions in the lift force, passively unloading large aerodynamic forces. These results indicate that the wing can sustain a relatively constant airfoil shape and lift coefficient for wind speeds below 7.83 m s^{-1} while supplying load alleviation in higher aerodynamic force environments, thus minimizing unwanted changes in vertical acceleration. We showed that the flexible airfoil's response was primarily due to increasing Reynolds number and thus flow speed, with little effect from changes in angle of attack. Passive aerodynamic unloading occurs instantaneously in response to changes in aerodynamic forces, providing to other forms of unloading which rely on controllers and actuators.

Upon modeling the response of the feather as a flexible trailing edge, the chordwise stiffness properties were reverse engineered to achieve the same aeroelastic effect in a 3D printed wing. The solution showed that the non-uniform stiffness properties of the feather can be easily replicated. In fact, the solution map showed that this could be accomplished through many different combinations of Young's moduli and trailing edge thickness. This solution

flexibility allows for replication regardless of multi-material 3D printing capabilities. This demonstrated that the chordwise stiffness of the feather can be replicated with either a single Young's modulus with a customized thickness, or using both tailored Young's modulus and thickness.

Overall, the research presented here sheds light on the physics of how feather-inspired compliant wings interact with load disturbances by modeling and clarifying the relevant FSI. Future work will focus on assessing dynamic wind gusts to provide a more complete understanding of the aero-structural characteristics in turbulent environments. Furthermore, future work may include expanding the modeled physics to include the effects of overlapping feathers and the vane's structural properties. Wind tunnel testing of both the biological and the engineered flexible trailing edge is also planned to further verify that these effects can be reproduced in an engineering setting.

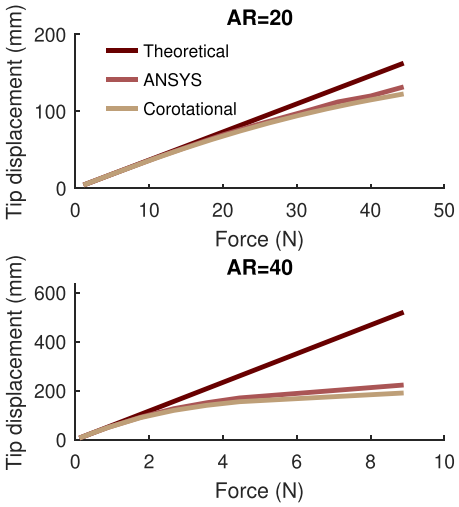

Figure A1. Comparison between theoretical, analytical ANSYS, and corotational model for beam of aspect ratio 20 and 40.

Acknowledgments

This work is supported in part by the US Air Force Office of Scientific Research under Grant Number FA9550-16-1-0087, titled 'Avian-Inspired Multifunctional Morphing Vehicles' monitored by Dr. BL Lee, and by the NSF Emerging Frontiers in Research and Innovation under Grant Number 1935216 titled 'Integration of Avian Flight Control Strategies with Self Adaptive Structures for Stable Flight in Unknown Flows'. Additionally, the authors would like to acknowledge Bret Tobalske at the University of Montana for kindly providing the red-tailed hawk feathers that were scanned in this work.

Appendix A. Model validation

We validated the structural, fluid, and XCO model individually to assess the accuracy of the entire model. First, the corotational beam method was validated against ANSYS Mechanical numerical simulations and a theoretical beam model. Next, the XFOIL model was validated against experimental data and an ANSYS Fluent numerical simulations using a low Re turbulence model. Lastly, the XCO developed in this work was validated against an ANSYS 2-way coupled FSI model.

A.1. Structural validation

We conducted the structural validation for a cantilevered beam with a square cross section, a length of 254 mm, a Young's modulus of 689.5 MPa and a tip loading of 0 to 44.5 N. The analysis was conducted for beams of aspect ratios 20 and 40 where, for a square cross section, the aspect ratio is defined as the beam length divided by the beam height. This corresponds to beam heights of 6.4 mm and 12.7 mm, respectively. The ANSYS model utilized 1×10^3 quadrilateral elements. Euler–Bernoulli beam theory was used as the theoretical model and is detailed below.

$$\delta = PL^3/EI \tag{A.1}$$

where δ represents the beam's tip displacement, P represents the magnitude of the tip loading, and L represents the beam's length.

The results of the validation are presented in figure A1. As expected, the theoretical model does a poor job at predicting the nonlinear behavior. This is especially evident as the deflection increases, where nonlinear effects are well known to dominate the response. However, the corotational beam theory and the ANSYS numerical model show very good agreement up to large displacements. At a tip displacement of 127 mm, the error between the ANSYS and corotational solution was 7% and 5% for the 20 and 40 aspect ratio beams, respectively (figure A1). As a 127 mm tip displacement represents 50% of the beam's length and is well above any expected feather deformation, these accuracies are excellent.

A.2. Fluid validation

Reynolds-averaged Navier–Stokes (RANS) simulations using ANSYS Fluent were conducted to validate the XFOIL model for an NACA 6409 airfoil at a Reynolds number of 2×10^5, which is in the mid range of Reynolds numbers tested in the complete analysis. This corresponds to approximately the upper Re limit of bird flight. The two-equation $k - \omega$ shear stress transport (SST) turbulence model was implemented, as this class of models is well known for their robustness and superior low Re performance [45, 54]. The SST model in particular exhibits superior prediction of the onset and degree of flow separation and has demonstrated good agreement with other high lift low Re airfoils [55]. Here, we assume incompressible flow and the equations are solved using a pressure-based

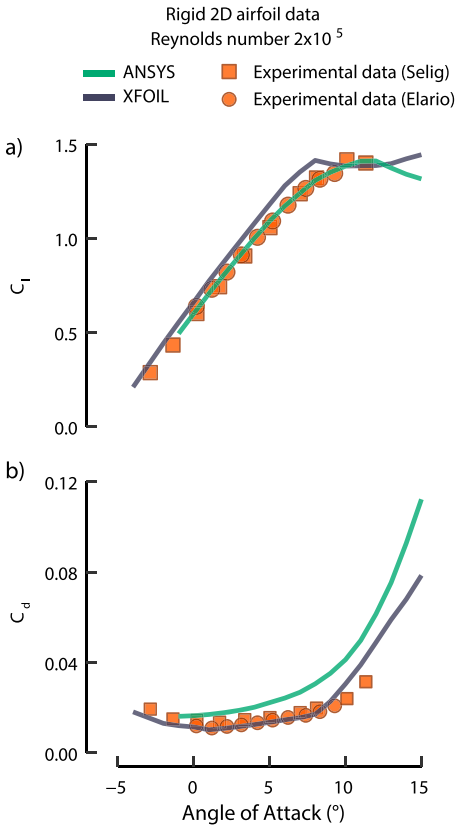

Figure A2. Lift and drag comparisons between experimental data [48], XFOIL, ANSYS for a rigid NACA 6409 airfoil.

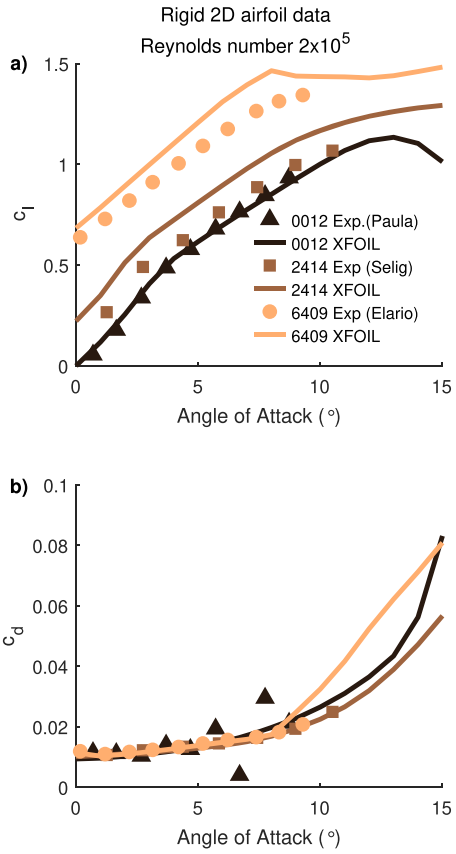

Figure A3. Lift and drag comparisons between XFOIL and experimental results for the NACA 0012 [57], NACA 2414 [58], and NACA 6409 [59] airfoils at a Reynolds number of 2×10^5.

solver accordingly. Furthermore, a coupled algorithm was implemented which typically offers better performance than segregated algorithms. The flow around the airfoil was simulated with a C-type mesh domain where the inlet and outlet boundaries were set to be 15 and 30 chord lengths away from the airfoil, respectively. A no-slip condition was imposed at the airfoil surface. The SST model requires boundary layer resolution larger than 10 grid points; thus, we aimed to achieve 30 points in the near-wall flow for the purpose of this simulation. The inlet was prescribed a turbulence intensity of 0.2%.

These results show fairly good agreement between the experimental data, ANSYS, and XFOIL (figure A2). The data show exceptional agreement between the ANSYS model and the experimental lift data, while the experimental drag data was more accurately simulated by XFOIL. Drag is an incredibly sensitive parameter both when experimentally measuring and numerically simulating it. These findings mirror the trends mentioned in section 3.1, notably, XFOIL over predicts the lift and under predicts the drag, which mirrors observed low Re trends [42]. The maximum error in lift between XFOIL and experiments is 11.5% which is acceptable for rapid low-fidelity simulations. It should also be noted that replicating wind tunnel results at low Re is notoriously difficult due to discrepancies in turbulence, wall effects, and boundary layer effects [56]. As such, the results of this analysis should be viewed as a validation that the simulation provides a reasonable approximation of the magnitude, but good approximation of the trends.

A.2.1. Effects of airfoil choice

Although the XFOIL simulation experiences up to 11.5% error, this is dependent upon the airfoil's geometry, as XFOIL is able to predict other airfoil geometries more accurately. That is to say, the errors in our simulations could be decreased by using a different airfoil as our base geometry. This is visualized in figure A3 which demonstrates that XFOIL has excellent agreement with experimental results for a NACA0012 airfoil, moderate agreement for an NACA 6900 airfoil especially at low angles of attack, and subpar agreement for an NACA 2414 airfoil at $\mathrm{Re} = 2 \times 10^5$. We performed a comprehensive analysis which led us to choose the NACA 6409 airfoil for this work.

The following criteria factored into our decision: bioinspired geometry, likelihood of agreement with experiments, success of convergence, and availability of experimental data for validation and comparison. To mimic a bioinspired geometry, our final airfoil needed to be moderately to highly cambered, moderately thin, and with a maximum camber towards

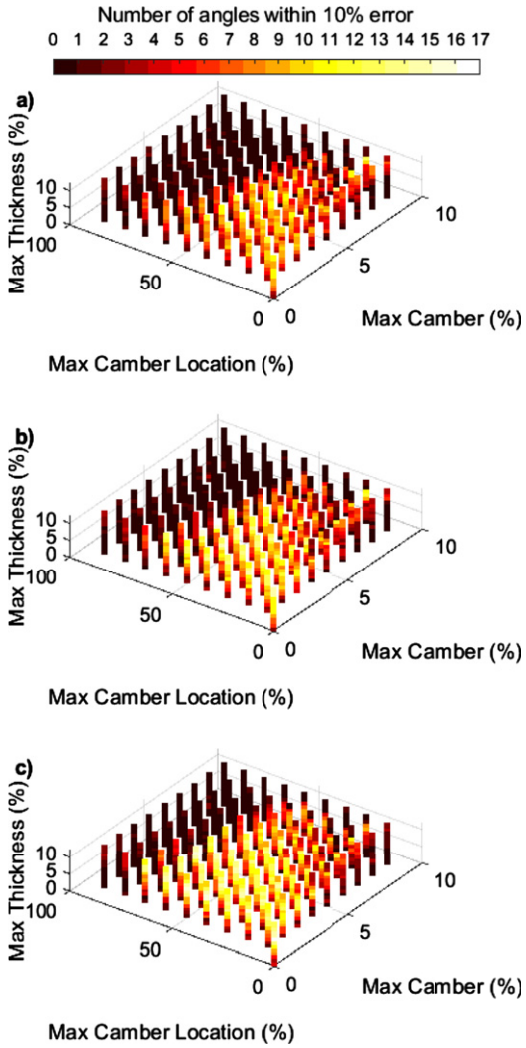

Figure A4. Agreement between inviscid and viscous solutions for NACA airfoils at (a) 2×10^5, (b) 3×10^5 and (c) 5×10^5 Reynolds numbers.

the leading edge or center of the airfoil. To assess the likelihood of agreement with experiments, we compared the viscous and inviscid solutions from our XFOIL model for 1092 different 4-digit NACA airfoils at 3 different Reynolds numbers ($2 \times 10^5, 3 \times 10^5$, and 5×10^5). The airfoils were categorized based on how many angles of attack were within 10% of the inviscid solution. This allows us to reduce the search space by eliminating airfoils where the viscous response is heavily influenced by the geometry (figure A4). This method is meant to rapidly assess a vast range of airfoil shapes to determine which ones are likely to show good convergence and agreement with experiments.

As would be expected, higher Reynolds numbers show closer agreement between the viscous and inviscid solutions, since the low Re flow is dominated by viscous effects. Poor agreement occurs when the maximum camber is located towards the trailing edge of the flier (near 100% maximum camber location) regardless of Reynolds number. Furthermore, agreement typically decreases as the camber increases. Lastly, airfoils with moderate thickness demonstrate the best agreement, as very thin airfoils show very poor agreement and thicker airfoils begin to show less agreement. The effects of the latter are stronger at low Re. Among the airfoils with the best agreement, the NACA6409 was sufficiently bioinspired (moderately thick and cambered with the location of maximum camber away from the trailing edge), showed one of the best agreement across all three Reynolds numbers with agreement within 10% for 9, 12, and 13 angles of attack, respectively, and has relatively consistent experimental wind tunnel data available at our Reynolds numbers of interest.

A.3. Coupled validation

The XCO model detailed in section 3.4 was validated using ANSYS. The ANSYS structural and fluid models validated in the prior sections were coupled using steady state 2-way system coupling. We aimed to reproduce the structural properties assumed in the numerical model. As noted previously, the airfoil's surface geometry strictly serves to influence the aerodynamic loadings while the flight feathers are assumed to carry the trailing edge loads. Thus, when recreating the structural model in ANSYS, a solution was devised to minimize the structural stiffness of the trailing edge airfoil that surrounded the feather rachis. This was accomplished by simulating the material properties of the surrounding airfoil as a hydrogel which exhibits a very low Young's modulus, multiple orders of magnitude less than that of the rachis. The system coupling was finalized with dynamic meshing which was enforced at the fluid–structure interface and updated each iteration. In total, the coupled simulation underwent 50 coupling steps and each coupling step underwent 20 fluid iterations. The fluid residuals were set to reach 1×10^{-5} each fluid iteration, while the mechanical solver was allowed to determine convergence given the number of substeps needed for each coupling iteration. The coupled solution was said to have converged when $\log_{10}$ RMS < -2.

The results of the validation are shown in figure A5. The lift and drag for both XCO and ANSYS models show similar trends to that of the rigid airfoil. The XCO model predicts a larger lift coefficient and a smaller drag coefficient than ANSYS which mirrors our findings in A2. These results indicate that flexibility does not create notable differences in the aerodynamics between the two models at this Reynolds number. Prior to the XCO stall angle, where the lift coefficient is at its maximum, the predicted tip displacements are in very good agreement with less than 12.4% error. This error is largely due to XFOIL overpredicting the lift. The tip displacements predicted from XCO experience stall-like behavior. Past the angle of maximum lift, the tip displacement experiences a sharp reduction before increasing again. This

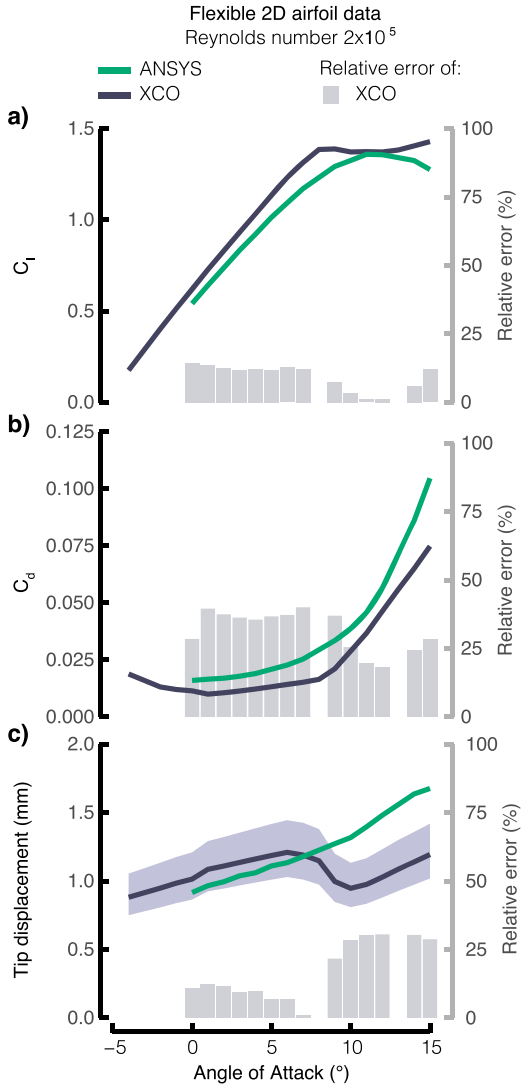

Figure A5. Lift, drag, and displacement comparisons between XFOIL and ANSYS models of a bioinspired flexible airfoil.

is due to the strong influence of the aerodynamic force on the total displacement. Interestingly, this trend is not observed in the ANSYS results and is accountable for the post-stall increase in relative error.

The shaded bands, included in the XCO lift, drag, and displacement plots, represent the experimental variation in the rachis material properties. This was obtained by calculating the minimum and maximum bending stiffness from the standard deviation ($N = 6$) provided with the rachis material properties [34]. These bands can be interpreted as the effects of variation within a species. The effects are indistinguishable on the lift and drag profiles but are prominent in the displacement response. One interesting observation is that the error observed between the XCO and ANSYS tip displacements falls within the displacement range due to species variation.

To summarize, the results of the validation presented in this section demonstrate that the XCO model reasonably predicts the aerodynamic and structural response prior to the stall angle. Much of the discrepancy is attributed to XFOIL which is known to over predict the lift at low Re. However, the power of the XCO model lies in its computational efficiency. Whereas the ANSYS FSI model requires extraordinary computational power and hours of computational time to calculate the coupled interactions for a single angle of attack, the XCO model takes a matter of seconds. This allows for rapid analysis across a range of flight conditions and readily enables design and optimization without the use of supercomputing.

Appendix B. Bibliography

ORCID iDs

Lawren L Gamble https://orcid.org/0000-0002-9568-9562
Christina Harvey https://orcid.org/0000-0002-2830-0844
Daniel J Inman https://orcid.org/0000-0001-6195-1334

References

[1] Gamble L L and Inman D J 2017 Why morphology matters in birds and UAV's: how scale affects attitude wind sensitivity *Appl. Phys. Lett.* **111** 203701
[2] Alerstam T, Rosén M, Bäckman J, Ericson P G P and Hellgren O 2007 Flight speeds among bird species: allometric and phylogenetic effects *PLoS Biol.* **5** 1656–62
[3] Pennycuick C J and Webbe D 1959 Observations on the fulmar in Spitsbergen *Br. Birds* **52** 321–32
[4] Hankin E H 1913 *Animal Flight: a Record of Observation* (London: Iliffe & Sons Limited) https://doi.org/10.1017/S2398187300140083
[5] Tucker V A 1987 Gliding birds: the effect of variable wing span *J. Exp. Biol.* **133** 33–58
[6] Gillies J A, Thomas A L and Taylor G K 2011 Soaring and manoeuvring flight of a steppe eagle *Aquila nipalensis J. Avian Biol.* **42** 377–86
[7] Harvey C, Baliga V B, Lavoie P and Altshuler D L 2019 Wing morphing allows gulls to modulate static pitch stability during gliding *J. R. Soc. Interface* **16** 20180641
[8] Durston N E, Wan X, Liu J G and Windsor S P 2019 Avian surface reconstruction in free flight with application to flight stability analysis of a barn owl and peregrine falcon *J. Exp. Biol.* **222** 185488
[9] Kaul U K and Nguyen N T 2018 Drag characterization study of variable camber continuous trailing edge flap *J. Fluid Eng.* **140** 101108
[10] Pankonien A M and Inman D J 2015 Spanwise morphing trailing edge on a finite wing *Active and Passive Smart Structures and Integrated Systems* vol 9431 (International Society for Optics and Photonics) p 94310T
[11] Woods B K, Bilgen O and Friswell M I 2014 Wind tunnel testing of the fish bone active camber morphing concept *J. Intell. Mater. Syst. Struct.* **25** 772–85
[12] Pankonien A M, Faria C T and Inman D J 2015 Synergistic smart morphing aileron: experimental quasi-static performance characterization *J. Intell. Mater. Syst. Struct.* **26** 1179–90
[13] Blower C J and Wickenheiser A M 2011 Two-dimensional localized flow control using distributed, biomimetic feather structures: a comparative study *Bioinspiration, Biomimetics, and Bioreplication* vol 7975 (International Society for Optics and Photonics) p 79750L

[14] Gamble L L, Pankonien A M and Inman D J 2016 Stall recovery of the span-wise morphing trailing edge concept via an optimized nonlinear model *Proceedings of the 26th International Conference on Adaptive Structures and Technologies* (New York: Curran Associates) pp 36–49

[15] Maeda M, Nakata T, Kitamura I, Tanaka H and Liu H 2017 Quantifying the dynamic wing morphing of hovering hummingbird *R. Soc. Open Sci.* **4** 170307

[16] Bakhtian N, Babinsky H, Thomas A and Taylor G 2007 The low Reynolds number aerodynamics of leading edge flaps *45th AIAA Aerospace Sciences Meeting and Exhibit* (Reno: American Institute of Aeronautics and Astronautics) pp 662

[17] Lynch M, Mandadzhiev B and Wissa A 2018 Bioinspired wingtip devices: a pathway to improve aerodynamic performance during low Reynolds number flight *Bioinspiration Biomimetics* **13** 036003

[18] Tucker V A 1993 Gliding birds: reduction of induced drag by wing tip slots between the primary feathers *J. Exp. Biol.* **180** 285–310

[19] Bachmann T, Blazek S, Erlinghagen T, Baumgartner W and Wagner H 2012 Barn owl flight '*Nature-Inspired Fluid Mechanics*' (Nature-Inspired Fluid Mechanics: Results of the DFG Priority Programme 1207 2006-2012) ed C Tropea and H Bleckmann (Berlin: Springer) pp 101–17

[20] Nachtigall W and Wieser J 1966 Profilmessungen am Taubenflügel *Z. Vgl. Physiol.* **52** 333–46

[21] Kim S H and Lee I 1996 Aeroelastic analysis of a flexible airfoil with a freeplay non-linearity *J. Sound Vib.* **193** 823–46

[22] Levin O and Shyy W 2001 Optimization of a flexible low Reynolds number airfoil *39th Aerospace Sciences Meeting and Exhibit* (Reno, U.S.A.: American Institute of Aeronautics and Astronautics) https://doi.org/10.2514/6.2001-125

[23] Shyy W, Smith R, Shyy W and Smith R 1997 A study of flexible airfoil aerodynamics with application to micro aerial vehicles *28th Fluid Dynamics Conference Snowmass Village* (CO, U.S.A.: American Institute of Aeronautics and Astronautics) https://doi.org/10.2514/6.1997-1933

[24] Shyy W, Berg M and Ljungqvist D Jul Flapping and flexible wings for biological and micro air vehicles *Prog. Aerosp. Sci.* **35** 455–505

[25] Lian Y and Shyy W 2007 Laminar-turbulent transition of a low Reynolds number rigid or flexible airfoil *AIAA J.* **45** 1501–13

[26] Tang J, Viieru D and Shyy W 2007 A study of aerodynamics of low Reynolds number flexible airfoils *37th AIAA Fluid Dynamics Conference and Exhibit* p 4212

[27] Heathcote S and Gursul I 2007 Flexible flapping airfoil propulsion at low Reynolds numbers *AIAA J.* **45** 1066–79

[28] Bansmer S, Radespiel R, Unger R, Haupt M and Horst P 2010 Experimental and numerical fluid–structure analysis of rigid and flexible flapping airfoils *AIAA J.* **48** 1959–74

[29] Relvas A and Suleman A 2007 Application of the corotational structural kinematics and Euler flow to two-dimensional nonlinear aeroelasticity *Comput. Struct.* **85** 1372–81

[30] Lian Y, Shyy W, Viieru D and Zhang B 2003 Membrane wing aerodynamics for micro air vehicles *Prog. Aerosp. Sci.* **39** 425–65

[31] Hu H, Tamai M and Murphy J T 2008 Flexible-membrane airfoils at low Reynolds numbers *J. Aircr.* **45** 1767–78

[32] Förstching H and Hennings H 2012 Aeroelastic mysteries in avian flight *CEAS Aeronaut. J.* **3** 135–43

[33] Hieronymus T L 2016 Flight feather attachment in rock pigeons (Columba livia): covert feathers and smooth muscle coordinate a morphing wing *J. Anat.* **229** 631–56

[34] Bachmann T, Emmerlich J, Baumgartner W, Schneider J M and Wagner H 2012 Flexural stiffness of feather shafts: geometry rules over material properties *J. Exp. Biol.* **215** 405–15

[35] Purslow P P and Vincent J F V 1978 Mechanical properties of primary feathers from the pigeon *J. Exp. Biol.* **72** 251–60

[36] Bonser R and Purslow P 1995 The Young's modulus of feather keratin *J. Exp. Biol.* **198** 1029–33

[37] Ennos A, Hickson J and Roberts A 1995 Functional morphology of the vanes of the flight feathers of the pigeon Columba livia *J. Exp. Biol.* **198** 1219–28

[38] Laboratory USFaWSF The feather atlas- feather identification and scans- available from: https://fws.gov/lab/featheratlas/feather.php?Bird&tnqx3d;BNOWprimary_male

[39] Murua J, Palacios R and Peiró J 2010 Camber effects in the dynamic aeroelasticity of compliant airfoils *J. Fluid Struct.* **26** 527–43

[40] Sucipto T, Berci M and Krier J 2013 Gust response of a flexible typical section via high-and (tuned) low-fidelity simulations *Comput. Struct.* **122** 202–16

[41] Drela M 1989 XFOIL: an analysis and design system for low Reynolds number airfoils *Low Reynolds Number Aerodynamics* (Berlin: Springer) pp 1–12

[42] Coder J G and Maughmer M D 2014 Comparisons of theoretical methods for predicting airfoil aerodynamic characteristics *J. Aircr.* **51** 183–91

[43] Genç M S, Kaynak and Lock G D 2009 Flow over an aerofoil without and with a leading-edge slat at a transitional Reynolds number *Proc. Inst. Mech. Eng.* G **223** 217–31

[44] Carruthers A C, Walker S M, Thomas A L R and Taylor G K 2010 Aerodynamics of aerofoil sections measured on a free-flying bird *Proc. Inst. Mech. Eng.* G **224** 855–64

[45] Hübbe G B B 2017 *Numerical and experimental anlysis of a high Lifting airfoil at Low reynolds number flows* Masters in Mechanical Engineering (San Catarina, Brazil: Federal University of Santa Catarina)

[46] Bachmann T 2010 *Anatomical, Morphometrical and Biomechanical Studies of Barn Owls' and Pigeons' Wings* (Aachen, Germany: RWTH Aachen University)

[47] Mueller H C, Berger D D, Mueller N S, Robichaud W and Kaspar J L 2004 Age differences in wing loading and other aerodynamic characteristics of red-tailed hawks *Wilson J. Ornithol.* **116** 272–4

[48] Selig M S 1995 *Summary of Low Speed Airfoil Data* (Ann Arbor, MI: SoarTech Publications)

[49] Heathcote D J, Gursul I and Cleaver D J 2018 Aerodynamic load alleviation using minitabs *J. Aircr.* **55** 2068–77

[50] Arrieta A F, Bilgen O, Friswell M I and Hagedorn P 2012 Passive load alleviation bi-stable morphing concept *AIP Adv.* **2** 032118

[51] Sunada S, Sakaguchi A and Kawachi K 1997 Airfoil section characteristics at a low Reynolds number *J. Fluid Eng.* **119** 129–35

[52] Abbott I H and Aev D 2012 *Theory of Wing Sections: Including a Summary of Airfoil Data* (Chelmsford, MA: Courier Corporation)

[53] Slesarenko V and Rudykh S 2018 Towards mechanical characterization of soft digital materials for multimaterial 3D-printing *Int. J. Eng. Sci.* **123** 62–72

[54] Bardina J, Huang P and Coakley T 1997 Turbulence modeling validation, testing, and development available from: https://ntrs.nasa.gov/search.jsp?R&tnqx3d;19970017828

[55] Menter F 1994 Two-equation Eddy-viscosity turbulence models for engineering applications *AIAA J.* **32** 1598–605

[56] Lissaman P B S 1983 Low-Reynolds-number airfoils *Annu. Rev. Fluid Mech.* **15** 223–39

[57] Paula A A 2016 *The Airfoil Thickness Effects on Wavy Leading Edge Phenomena at Low Reynolds Number Regime* (São Paulo: Universidade de São Paulo)

[58] Selig M S and Beach V 1996 *Summary of Low Speed Airfoil Data* vol 2 (Ann Arbor, MI: SoarTech Publications)

[59] Elario D S G 1991 NASA advanced aeronautics design solar powered remotely piloted vehicle *Technical Report* No. NASA-CR-190007, NAS 1.26:190007 NASA